# Modeling Dissolved and Particulate Th in the Canada Basin: Implications for Recent Changes in Particle Flux and Intermediate Circulation

Xiaoxin Yu, Susan Allen, Roger François, Mélanie Grenier, Paul Myers, Xianmin Hu

JGR Oceans

RESEARCH ARTICLE
10.1029/2019JC015640

# Modeling Dissolved and Particulate $^{230}$Th in the Canada Basin: Implications for Recent Changes in Particle Flux and Intermediate Circulation

**Xiaoxin Yu[1], Susan E. Allen[1], Roger François[1], Mélanie Grenier[1], Paul G. Myers[2], and Xianmin Hu[2]**

[1]Department of Earth, Ocean and Atmospheric Sciences, University of British Columbia, Vancouver, British Columbia, Canada, [2]Department of Earth and Atmospheric Sciences, University of Alberta, Edmonton, Alberta, Canada

**Key Points:**

- $^{230}$Th concentration in Canada Basin has decreased due to enhanced productivity and due to increased exchange between margins and interior
- Including additional scavenging near the sea floor, the model better reproduces the observed $^{230}$Th and its changes over the last two decades
- Use of $^{230}$Th model, combined with observations, elucidates changes in the Arctic intermediate circulation

**Correspondence to:**
S. Allen,
sallen@eoas.ubc.ca

**Citation:**
Yu, X., Allen, S. E., Francois, R., Grenier, M., Myers, P. G., & Hu, X. (2020). Modeling dissolved and particulate $^{230}$Th in the Canada Basin: Implications for recent changes in particle flux and intermediate circulation. *Journal of Geophysical Research: Oceans*, *125*, e2019JC015640. https://doi.org/10.1029/2019JC015640

Received 12 SEP 2019
Accepted 25 JAN 2020
Accepted article online 20 FEB 2020



**Abstract** Global climate change has had large impacts on the Arctic region including rapid reductions in sea ice and rapid increases in surface air temperatures. Documenting the consequences of these changes in the Arctic Ocean is difficult, however, because accessibility limits observations in space and time and aliases measurements. This problem can be alleviated by using geochemical tracers, which can act as natural integrators, allowing us to determine net changes over regions and years. One such tracer is $^{230}$Th. We use measurements and an off-line scavenging model forced by ANHA4, a regional configuration of the NEMO general circulation model, to investigate changes in the Canada Basin in the years 2002–2015. Observations show a clear decrease in $^{230}$Th in intermediate layers, particularly in the internal Canada Basin. The model reproduces the observed changes in $^{230}$Th concentration profiles. Using the model to determine the origin of the reduction shows that the decrease is due to both higher particle fluxes from increased productivity resulting from the reduction in sea ice cover and increased circulation and stirring by mesoscale eddies increasing lateral exchange between the productive coastal regions and less productive internal Canada Basin. The circulation model clearly shows increased velocities as the ice cover has decreased and storms have increased.

## 1. Introduction

The Arctic Ocean is experiencing climate change more rapidly than lower latitude regions (Core Writing Team, 2014). Beginning from the late 1990s, the summer ice extent has decreased by more than 35% (Serreze et al., 2016). Decreases in summer ice have both increased biological productivity (Arrigo et al., 2008) and, potentially, increased mixing in the Arctic Ocean. $^{230}$Th, a geochemical tracer with a residence time well matched to decadal variation in the Arctic Ocean, is applied in this study. Observations have shown dramatic changes in the Arctic $^{230}$Th profiles since the 1980s (Grenier et al., 2019). Here we focus on the Atlantic layer of the Canada Basin and use a $^{230}$Th scavenging model coupled to an Arctic Ocean circulation model, to elucidate the ocean dynamics leading to the observed changes.

The Atlantic layer, also known as the intermediate layer in the Arctic, is considered to be the layer between isopycnal $\sigma_\theta = 27.8$ at around 400 m and isopycnal $\sigma_\theta = 28.0$ at around 1,500 m (Lique et al., 2010). In this layer, the residence time scale of the water in the Arctic Ocean is on the order of 30 years (Lique et al., 2010). The Atlantic layer is warm compared to layers above and below and, if mixed to the surface, could melt much of the remaining ice in the Arctic Ocean (Rudels et al., 2004). Large changes in this layer have been measured both in its warmth and its flux (McLaughlin et al., 2009), and observations also suggest changes in circulation patterns (Grenier et al., 2019; Karcher et al., 2012; McLaughlin et al., 2009). The main flow in the layer is through boundary currents (Woodgate et al., 2007), which are very narrow due to the small Rossby radius in the Arctic. As such, direct changes in circulation are difficult to measure and much of our knowledge is based on changes in water properties (Dosser & Timmermans, 2018; Karcher et al., 2012; McLaughlin et al., 2009; Woodgate et al., 2007).

Water tracers with strong contrasts between regions, either due to their inherent properties or due to a singular source, give a strong signal of flow changes. Scavenged tracers are sensitive to the sinking particle field and the residence time of water. The Arctic Ocean has strong variations in biological productivity, and these are changing in time (Arrigo et al., 2008). The strong coastal currents and weaker basin circulations

lead to variations in residence time with the shortest times in the boundary currents and the longest times under the thickest ice in the Alpha-Mendeleev Region (Tanhua et al., 2009). Here, we will focus on changes in the Canada Basin where there is a strong contrast in productivity and particle concentration between the continental shelf and the oligiotrophic Beaufort Gyre (Jackson et al., 2010). Thus, we observe strong contrasts in scavenged tracer $^{230}$Th (Grenier et al., 2019).

The scavenged tracer $^{230}$Th has been considered as a useful proxy in ocean circulation studies (Dutay et al., 2009; Marchal et al., 2007). With a scavenging residence time of two to four decades, it is commonly coupled with $^{231}$Pa, which is less particle reactive and thus has a longer residence time (Anderson et al., 1983; Bacon, 1988), to understand large-scale ocean processes such as the overturning circulation (Yu et al., 1996). However, as the residence time scale of the Atlantic layer in the Arctic Ocean is more consistent with that of $^{230}$Th, we use $^{230}$Th alone in this study.

Produced by the decay of $^{234}$U, $^{230}$Th is added in the ocean at a constant rate. It is rapidly scavenged onto sinking marine particles, reversibly; it can desorb from particles and return back to water column in dissolved form. Such exchange between two phases occurs continuously until the marine particles eventually reach the seafloor. This process will be referred as "scavenging" in the rest of the paper. Scavenging in still water, at steady state and with constant scavenging parameters (particle sinking speed and adsorption and desorption coefficients), leads to a characteristic linear, increasing profile with depth.

In addition to the scavenging process, the $^{230}$Th distribution is also controlled by physical processes, such as advection and mixing. The presence of such processes transports $^{230}$Th away from its production sites. If there is a large $^{230}$Th difference between the production site and the receiving waters produced by different scavenging intensities, the resulting $^{230}$Th profile will deviate from linearity.

The activities of the dissolved and particulate phases are thus governed by the following equations (Luo et al., 2010):

$$\frac{\partial x_d}{\partial t} = q - k_a x_d + k_d x_p + \text{advection} + \text{mixing} \tag{1}$$

$$\frac{\partial x_p}{\partial t} = k_a x_d - k_d x_p - s\frac{\partial x_p}{\partial z} + \text{advection} + \text{mixing} \tag{2}$$

where $x_d$ and $x_p$ are $^{230}$Th concentrations in dissolved and particulate forms respectively, $q$ (dpm m$^{-3}$ yr$^{-1}$) is the production rate of $^{230}$Th, $k_a$ (yr$^{-1}$) and $k_d$ (yr$^{-1}$) are the exchange rate constants of $^{230}$Th by adsorption and desorption, respectively, $s$ (m yr$^{-1}$) is the sinking speed of particles and $z$ (m) is vertical depth, positive upward. Note that these equations neglect the radioactive decay of $^{230}$Th itself, as $^{230}$Th's half-life (75,200 years) is much beyond the decadal time scale.

To produce a reasonable $^{230}$Th simulation, it is essential to catch large spatial variations and rapid temporal changes in the ocean productivity. Vertical and spatial variations are allowed in the scavenging coefficients inspired by previous studies (Dutay et al., 2009; Lerner et al., 2016). It has also been shown that additional bottom scavenging is needed (Rempfer et al., 2017). Based on these findings, we present the first three-dimensional, Arctic Ocean $^{230}$Th model and use it to facilitate the understanding of ocean circulation changes in the Arctic Ocean, especially in the Atlantic layer of the Canada Basin. This study also serves as an additional test of the robustness of $^{230}$Th as an ocean circulation tracer.

This paper is organized as follows: Section 2 describes sources of observational data, introduces the physical and the scavenging models, and describes model configuration for the different simulations (runs) we use. Section 3 first shows model and data comparison results, then further explores different tracer behaviors in the various simulations. The next section (section 4) discusses the performance of the tracer model, possible reasons for the observed decrease in $^{230}$Th concentration, and its implication to the underlying changes in Arctic Ocean circulation.

## 2. Methods

### 2.1. Data

We use observations from several sources: older published data (Bacon et al., 1989; Edmonds et al., 1998; Scholten et al., 1995; Trimble et al., 2004) and more recent data compiled by Valk et al. (2018) and Grenier et al. (2019). The more recent data were collected during six cruises: R/V *Polarstern* 2007 (GEOTRACES-IPY

**Table 1**
*Information for Recent $^{230}$Th Data*

| Reference | Year | Location | dissolved $^{230}$Th | total $^{230}$Th |
|---|---|---|---|---|
| Grenier et al. (2019) | 2007 | Amerasian Basin | Y | |
| Valk et al. (2018) | 2007 | Eurasian Basin | Y | Y |
| Grenier et al. (2019) | 2009 | Canada Basin | Y | |
| Grenier et al. (2019) | 2011 | Canada Basin | | Y |
| Grenier et al. (2019) | 2015 | Amerasian Basin | Y | |
| Valk et al. (2018) | 2015 | Eurasian Basin | Y | |

*Note.* Which were collected during R/V *Polarstern*, CCGS *Wilfred Laurier* cruises in 2007, CCGS *Louis St Laurent* cruise in 2011 and GEOTRACES cruises in 2009 and 2015. Note that total data are now available for the 2007 Amerasian and 2015 Eurasian cruises but were not used here.

section GIPY11) and 2015 (GEOTRACES section GN04), CCGS *Wilfried Laurier* 2007, CCGS *Louis St. Laurent* 2011, and GEOTRACES cruises 2009 (GEOTRACES-IPY section GPIY14) and 2015 (GEOTRACES section GN02) on the CCGS *Amundsen* (Table 1 and Figure 1). The analytical procedures followed to generate this data set are detailed in the above mentioned references. Most of these different analytical procedures were validated through successful participation of the labs in the GEOTRACES intercalibration exercise (Anderson et al., 2012). Moreover, the 2015 data from the Central Arctic Ocean and from the Canada Basin were validated through intercalibration of crossover stations with Robert Anderson's team at the Lamont-Doherty Earth Observatory of Columbia University (PhD student: Sebastián Vivancos; NY, USA).

Compared to salinity and temperature measurements, $^{230}$Th data are scarce in both temporal and spatial coverage. In this study, the $^{230}$Th data are separated into two groups to serve different purposes. The first group contains data from the older sources, which mainly cover the period of 1990s, and are used as the training samples to constrain the scavenging parameterization. The second group is the recent data collected after 2000 and is used to evaluate the $^{230}$Th model performance. To compare between model and data, we linearly interpolate in the vertical using the closest values above and below the required depth.

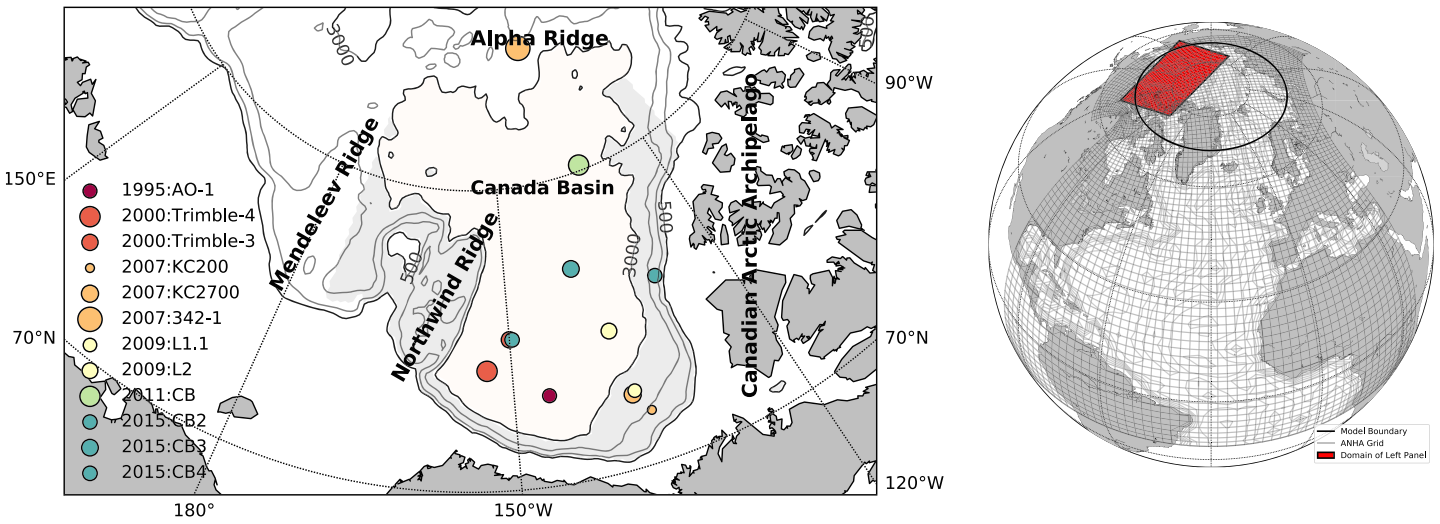


**Figure 1.** (left panel) Map of the Canada Basin with sampling locations. Samples from different cruises can be distinguished from the colors; the size of the points indicates the tracer concentrations at 500 m depth from vertical linear interpolation of closest values in the profile above and below that depth. Separated by isobath 3,000 m, the light gray area in the Canada Basin is defined as the "shallow region," while the area contained within by the dark 3,000 m isobath is considered the "deep basin." (right panel) Location of left panel map shown on the globe (red). Model grids and boundary locations of the ANHA4 configuration. The grid is plotted every 10 grid points. The contours are the bathymetry. The black circle at latitude 70°N delimits the tracer boundary.

### 2.2. Model

As the distribution of $^{230}$Th is controlled by both scavenging and physical processes, the typical way to simulate the tracer is to couple a chemical scavenging model to a physical model (Dutay et al., 2009; Luo et al., 2010; Marchal et al., 2000; Roy-Barman, 2009; Van Hulten et al., 2018).

#### 2.2.1. Physical Field

The physical model component is responsible for transporting and mixing tracers within the ocean. In this study, the dynamic fields we use are off-line ocean model results from the Arctic Northern Hemisphere Atlantic configuration (ANHA4, Courtois et al., 2017; Hu et al., 2018) for the Nucleus for European Modelling of the Ocean (NEMO) model (Madec & The NEMO team, 2016). NEMO includes a three-dimensional, free surface, hydrostatic, primitive-equation ocean general circulation model and a dynamic-thermodynamic sea ice model (Louvain-la-Neuve: LIM2). The physical model run was initialized by the Global Ocean Reanalyses and Simulations (GLORYS) data, forced by interannual atmospheric data from Canadian Meteorological Centre Global Deterministic Prediction System ReForecasts (CGRF) (Smith et al., 2014) and ran with interannual monthly runoff from Dai et al. (2009) until 2006, after which the monthly runoff averaged over October 1999 to September 2004 are used. NEMO v3.4 was used for this study using a $z$ coordinate with partial steps. The model was run without tides. Vertical mixing uses a turbulent kinetic energy dependent vertical diffusion (TKE) scheme parameterized using a 1.5 order turbulent closure scheme. The domain is bounded by open boundaries at 20°S latitude in the Atlantic Ocean and across the Bering Strait (Courtois et al., 2017; Hu et al., 2018) (Figure 1).

Data for model comparison in the Arctic Ocean is limited. This ANHA4 simulation has been evaluated using a number of metrics. It reproduces the large scale temperature and salinity structure in the Canada Basin well compared to data extracted from the World Ocean Atlas (Figure 2). It has been compared to other models in a recent Arctic intercomparison project (Ilicak et al., 2016; Wang et al., 2016a, 2016b) and lies close to the multimodel means.

The off-line ocean dynamics employed in the tracer model are 5-day means of horizontal and vertical velocity and vertical diffusivity from the ANHA4 configuration, which has a quarter-degree horizontal resolution (Figure 1) and 50 levels with layer thickness smoothly increasing from 1.05 m at the surface to 453 m at the deepest level. The tracer model was implemented using NEMO's off-line feature which uses the TOP framework. Total variation diminishing scheme (TVD) is used in calculating tracer advection. Vertical mixing uses the vertical diffusivity from the off-line run. Tracer lateral diffusion uses an isopycnal Laplacian operator with a horizontal eddy diffusivity of 300 $m^2\ s^{-1}$ as is used for salinity and temperature in the circulation model.

#### 2.2.2. Scavenging Model

Our second component is a reversible scavenging model that simulates the exchange processes between the dissolved and particulate form (Bacon & Anderson, 1982). Among the parameters in (1) and (2), the production rate $q$ is the only known parameter (0.0267 dpm $m^{-3}$ $yr^{-1}$); the rest (sinking speed $s$, scavenging coefficients $k_a$ and $k_d$) are left to be determined.

Our parametrization method for the unknown scavenging coefficient starts with the assumption that concentrations that linearly increase with depth are approximately at steady state and that for these profiles advection and mixing processes are negligible. This assumption allows us to estimate local coefficients for regions with linear profiles. We then take coefficients from a high summer ice region and from a low summer ice region, which we assume are low productivity/low particles and high productivity/high particle regions, respectively. We use these two sets to parametrize the coefficients in terms of minimum ice concentration in summer. Details follow.

To start, neglecting advection and mixing and assuming particulate $^{230}$Th is 0 at the surface, allows (1) and (2) to be combined as

$$x_p = \frac{q}{s} z \tag{3}$$

$$x_d = \frac{q}{k_a} + \frac{k_d}{k_a} \quad x_p = \frac{q}{k_a} + \frac{k_d q}{k_a s} z \tag{4}$$

The linearity of the steady-state analytical solutions, equations (3) and (4), enables us to estimate the scavenging coefficients through a least squares regression method. We are fortunate to have two sets of linear profiles: one from the low ice Eurasian Basin region and one from the high ice Alpha Ridge region

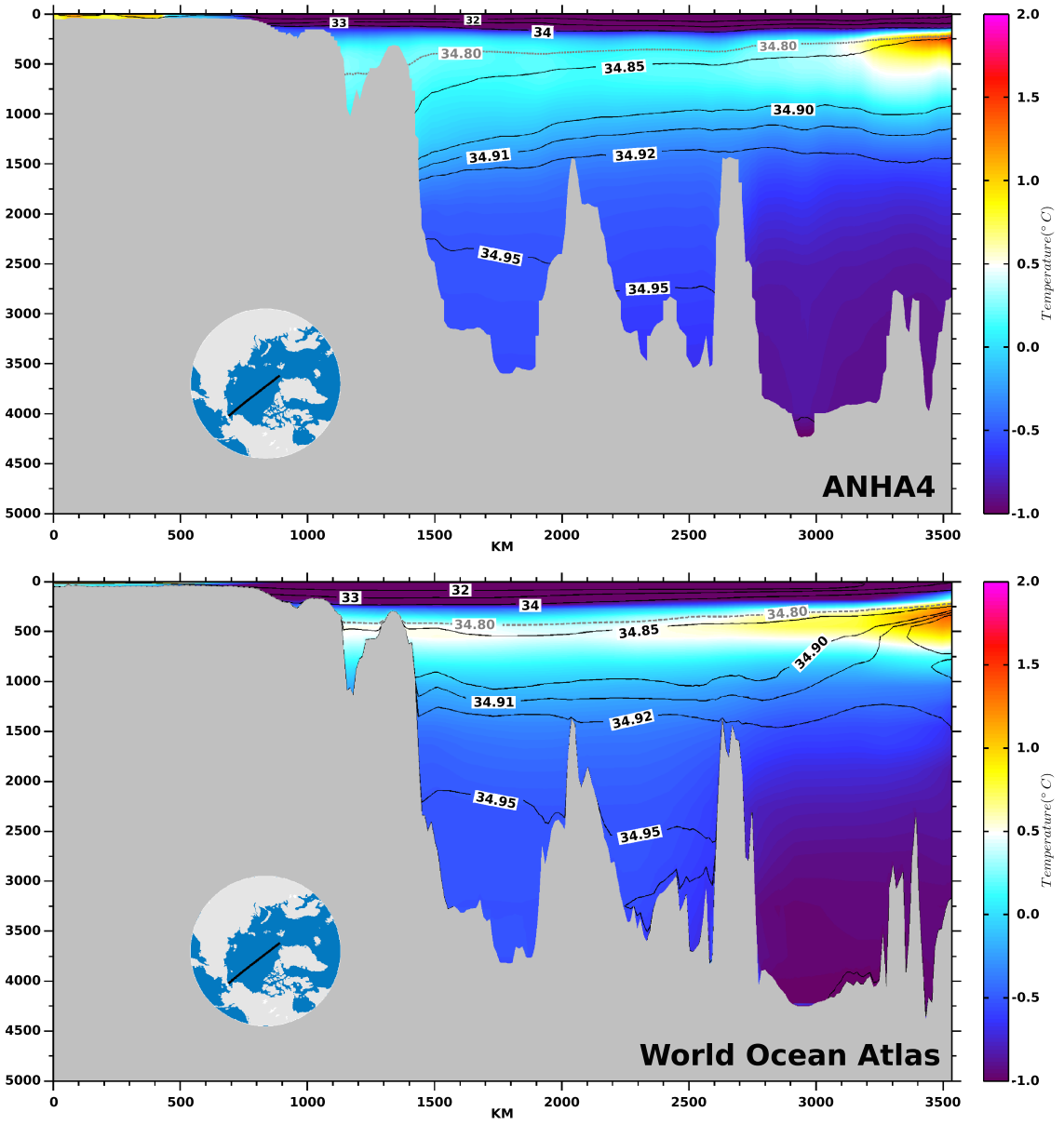


**Figure 2.** Comparison of ANHA4 (upper panel) to World Ocean Atlas (lower panel). Temperature (color) and salinity (black contours) cross sections, particularly across the Canada Basin, show good agreement with the depths of observed salinity and temperature layers. However, peak temperatures in the warm Atlantic layer at 500 m do decrease more quickly across the Arctic Ocean in the model than the observations.

(see Appendix A). These two regions have quite different sinking speeds and adsorption rates, which we assume are caused by differences in types and quantities of the particles scavenging $^{230}$Th. Particles vary over the Arctic Ocean due to a number of processes: biological productivity and ice concentration, included. As we expect a negative correlation between the Arctic Ocean productivity and sea ice concentration, and sea ice concentration is measured whereas accurate biological productivity is more difficult to obtain, we correlate scavenging coefficients with sea ice concentrations. Limited by the number of available linear profiles, our parametrization (Appendix A) gives a simple linear relationship between scavenging coefficients and sea ice concentrations:

$$s = s_0 - 987\, i \quad \mathrm{m\ yr^{-1}} \tag{5}$$

$$k_a = k_0 - 0.38i \quad \mathrm{yr^{-1}} \tag{6}$$
$$k_d = 0.8 \quad \mathrm{yr^{-1}}$$

where $i$ is the minimum summer sea ice concentration in units of fractional area. The intercept of the linear fit also provides the adsorption coefficient and sinking speed when there is no sea ice ($k_0 = 0.46$ yr$^{-1}$; $s_0 = 1,456$ m yr$^{-1}$), which is kept geographically uniform.

Lateral boundaries for the tracer model are at 70°N (Figure 1). Tracer values at the boundary are equal to initial conditions that are generated from published data compiled by Henderson and Wilkinson (2012) (see Yu, 2017). The surface boundary conditions for the particulate phase and dissolved phases are 0 and $q/k_a$, respectively. The bottom boundary uses a Neumann boundary condition so that the first derivative of the concentration between the deepest layer and the layer above is equal to that between the layer above and the layer above that.

We are essentially modeling one type of particles but are allowing their properties (i.e., $k_a$ and $s$) to vary spatially and temporally. The dominant particles scavenging $^{230}$Th are fine. These particles take multiple years to sink through the whole water column, equation (5). So year-to-year variations in summer productivity or summer sea ice concentration are not immediately reflected in the tracer profiles at deeper depths. To handle this process in the model we introduce another tracer variable, the ice fraction. This represents the type and concentration of particles, as determined by the ice fraction, when the particles are at the surface. As such, to complete the conjecture, it is important to take into consideration the sinking, advection and mixing motion of the particles:

$$\frac{\partial x}{\partial t} = s\frac{\partial x}{\partial z} + \vec{u} \cdot \nabla x + \text{mixing} \tag{7}$$

where $x$ is the ice fraction and $x$ at the surface is the ice fraction that was at the surface when the particles formed. Because particles that scavenge the tracer are assumed to move at the same speed as tracer's particulate form, the sinking speed, $s$, of particles produced at the surface under various sea ice covers is assumed to be identical to the sinking speed of the corresponding particulate tracer. The output from this model is called "pseudoparticle field" as it tracks the ice fraction that has an implicit relation to the particle concentration and type. This scheme is expected to capture the variation of scavenging in a changing Arctic Ocean.

The variation of sea ice concentration is crucial in setting the scavenging intensity in the Arctic Ocean. The modeled sea ice, in the Canada Basin, is biased high (Yu, 2017) so we use satellite-derived sea ice data from NOAA/NSIDC Climate Data Record data set (Meier et al., 2013; Peng et al., 2013) using results from the NASA team algorithm.

#### 2.2.3. Bottom Scavenging

Previous models have not included bottom scavenging (e.g., Luo & Lippold, 2015; Luo et al., 2010; Marchal et al., 2000). However, recent literature (Rempfer et al., 2017) and our preliminary model runs showed that bottom scavenging should not be neglected. In the Arctic Ocean, significant amounts of particles come from the continental margin and from a thick layer of water near the ocean bottom that contains large amounts of suspended sediment (known as the nepheloid layer). Observations suggest this layer is approximately 1,000 m thick in the Arctic Ocean (Hunkins et al., 1969). $^{230}$Th shows a change in profile slope at a similar depth, supporting an extra scavenging process within 1,000 m above the sea floor (Figure 3).

We did not want to increase the scavenging coefficients by simply doubling the normal scavenging strength (Rempfer et al., 2017), because scavenging is not spatially uniform in the Arctic Ocean. According to the $^{230}$Th data, we see spatial variations in the deep scavenging that are correlated with the ice concentration. There is less deep scavenging under thick ice but more deep scavenging beneath thin ice. So we apply a smooth function,

$$\gamma = 3(1 - i) \tag{8}$$

of sea ice concentration, $i$, to horizontally increase the scavenging intensity in the bottom layer. Vertically, the scavenging intensity within this special layer is set to smoothly increase to the amplified bottom strength. Note that the $\gamma$ function is only used in locations where the amplified scavenging intensity would not be too large; specifically, it is limited to be smaller than the ice free scavenging ($k_0$). The value 3 is chosen so that the maximum enhanced scavenging is just over 2 which is the value used in the previous study (Rempfer et al., 2017). In the bottom layer, the adsorption coefficient $k'$ is defined by

$$k_b = \min(k_0, (1 + \gamma)k_u) \tag{9}$$

**Table 2**
*Summary of the Numerical Runs*

| Simulation | Bottom scavenging | Forcing field | Sea ice |
|---|---|---|---|
| Base Run | yes | annual | annual |
| Exp. 1 | no | annual | annual |
| Exp. 2 | yes | constant | annual |
| Exp. 3 | yes | annual | constant |

$$k' = k_u + (k_b - k_u)\left(\frac{z - z_u}{z_b - z_u}\right)^2 \tag{10}$$

where subscript $b$ and $u$ represent the ocean bottom and upper limit (1,000 m above bottom), respectively. The formula for enhanced sinking speeds has the same form.

### 2.3. Overview of Experiments

Numerical models provide unique opportunities to differentiate the impact of distinct processes. Our base case is our best representation of actual conditions in Canada Basin over the simulation. The ANHA4 model (currents and mixing) includes the impacts of wind changes and ice changes on the circulation. The scavenging model (particles and $^{230}$Th) includes the impacts of ice changes on the particles: their sinking velocities and scavenging coefficients. Thus, by construction, the impact of ice on the circulation and the impact of ice on the particles can be separated. Note that the particles are forced by observed ice, not the ice from ANHA4.

Thus, in order to understand $^{230}$Th's response to processes such as bottom scavenging and changing ice conditions, we design a base run and three experimental runs (Table 2). While the Base Run has bottom scavenging and varying sea ice and ocean dynamics, Exp. 1 excludes the bottom component but shares the same forcing as Base Run; Exp. 2 keeps the extra scavenging components but the ocean dynamics are constant in time—the flow fields and mixing are repeats of Year 2002. Exp. 3 has the same ocean dynamics and bottom forcing as Base Run but uses a constant ice field, that of 2002, to determine the sinking particle properties. We use 2002 as our baseline to investigate recent changes as it is the earliest year for which we have the CGRF wind data. The model was spun-up for 12 years, nominally from 1991–2001 but as we did not have circulation fields for that span we used the 2002–2004 circulation repeated four times. For Exp. 1 and Exp. 2 the ice field was from 1991–2001. For Exp. 3 constant, 2002, ice was used.

## 3. Results

### 3.1. Effect of Bottom Scavenging

To facilitate interpretations of the $^{230}$Th simulations, we first present a model evaluation. Along with the evaluation, a comparison between runs with and without bottom scavenging is given to show the impact of extra scavenging in the nepheloid layer of the Arctic Ocean.

With the bottom scavenging excluded (Exp. 1), the model generally produces profiles that increase nearly linearly with depth (dashed profiles in Figure 3). Estimated tracer concentrations show good agreement with observations for the upper 1,000 m. Beneath this depth, the model tends to overestimate $^{230}$Th values. This discrepancy is especially obvious in the Nansen Basin (Figures 3m–3q) where the ice is thinner as the water is warmer (Muilwijk et al., 2016). In comparison, a noticeable difference in slopes of the vertical profiles is found in Base Run (solid profiles in Figure 3). With the bottom scavenging processes vertical gradients of the deep $^{230}$Th are reduced, bringing the model results much closer to the observations.

To quantitatively assess the improvement with nepheloid scavenging, we plot the model data against the observations (Figures 3y and 3z). The fit with the extra scavenging is significantly better with a slightly lower root-mean-square error (0.027 vs. 0.029) and the linear fit gives a slope closer to one. This improvement highlights the importance of having the bottom scavenging component in the $^{230}$Th model.

Estimates in the Nansen Basin (Figure 3z, orange circles) are generally too high, as is one profile near the Lomonosov Ridge (EB15, medium blue). Our focus here, however, is the Canada Basin where the model performs well and the data has significantly better spatial and temporal coverage.

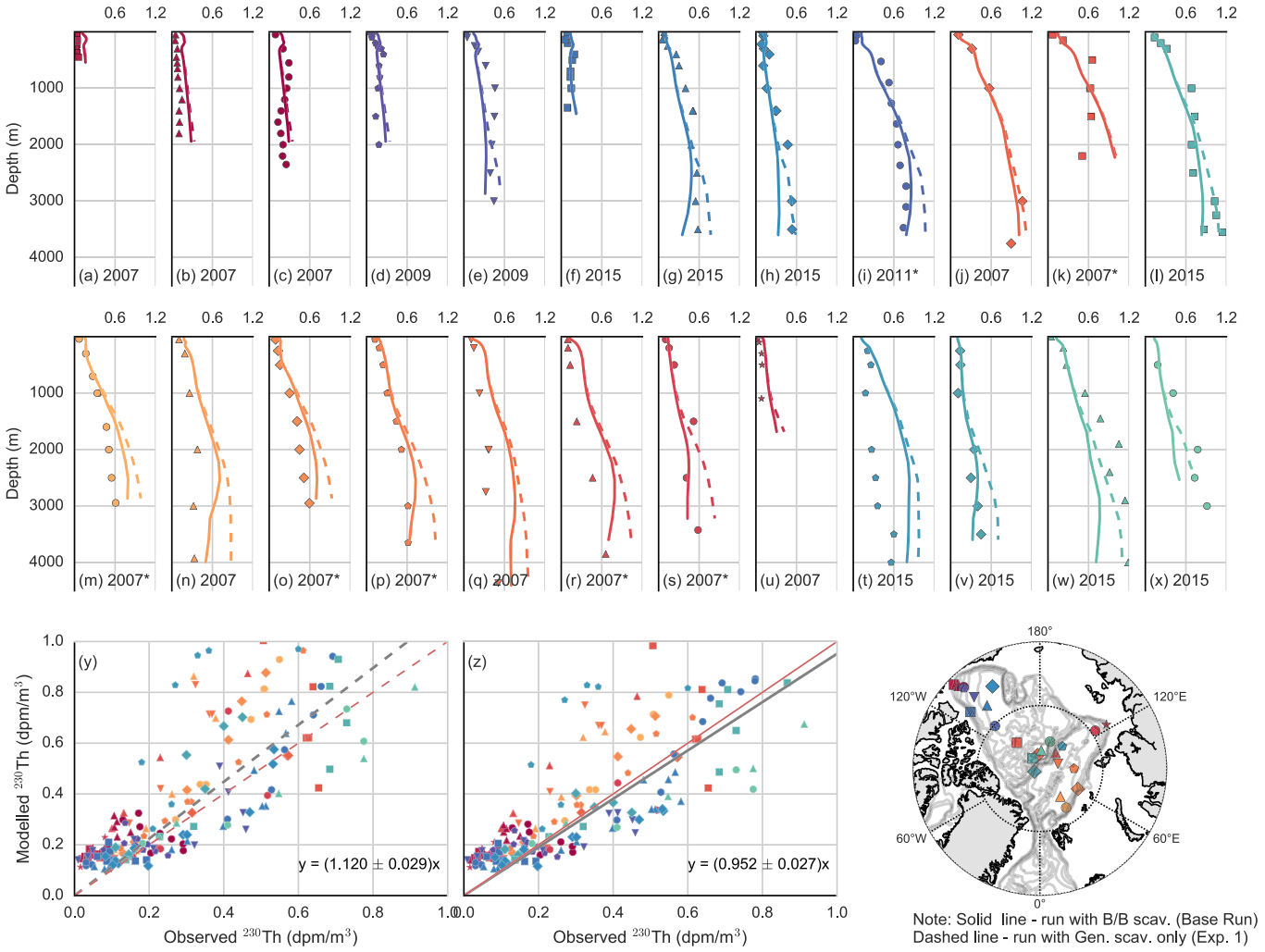


**Figure 3.** Observed versus modeled $^{230}$Th: upper two panels show profiles of model (lines) and observation (points). Note that solid lines are model results from the run with nepheloid scavenging (Base Run); dashed lines are from the run without nepheloid scavenging (Exp. 1). Plots marked with an asterisk (*) in label display total $^{230}$Th results; the rest are showing dissolved $^{230}$Th results. Colors and symbols of profiles match colors and symbols on map (lower right) and on scatter plots. Panels (a) to (x) are labeled with the year the profile was collected. Lower left plots (y and z) show a linear regression of observations versus simulations (gray line) and a one-to-one line to guide the eye (red line). Results from closest model points in the horizontal were interpolated vertically to the observational depth. Results suggest that the coupled circulation/Th model reproduces the observations at a desirable accuracy and that the bottom processes are one of the important components in allowing the model to achieve good agreement with observations.

### 3.2. Effect of Sea Ice and Mixing

We focus on the core of the Atlantic layer, specifically the layer between 496 and 590 m (nominal 500 m depth). Spatially, water masses in the south Canada Basin have lower $^{230}$Th than in the north (Figure 4) as ice free summers allow this part of the ocean to have higher biological productivity. A relatively high level of $^{230}$Th is found northeast of the Canada Basin near the Alpha Ridge (Figure 4). This region, covered by permanent ice, is known for having low primary productivity (e.g., Hill et al., 2013) and limited water exchange rates (Tanhua et al., 2009). Over the period 2002–2015, there is a substantial decrease in the basin-wide $^{230}$Th concentration at 500 m depth (Figure 4). This decrease in $^{230}$Th is also observed in profiles measured in 2015 (Figure 6 of Grenier et al., 2019). According to the model, by the end of 2015, the area with $^{230}$Th values higher than 0.3 dpm m$^{-3}$ is less than one third of that in 2002. The spatial gradient in the Canada Basin, especially in the southern part, has been significantly reduced.

As the concentration in the shallow coastal region (< 3,000 m depth) of the Canada Basin is significantly lower than that in the deep interior region (average depth 3,500 m), and the changes in those two regions appear different (Figures 4) we split the Canada Basin into these two regions for further analysis (Figure 1);

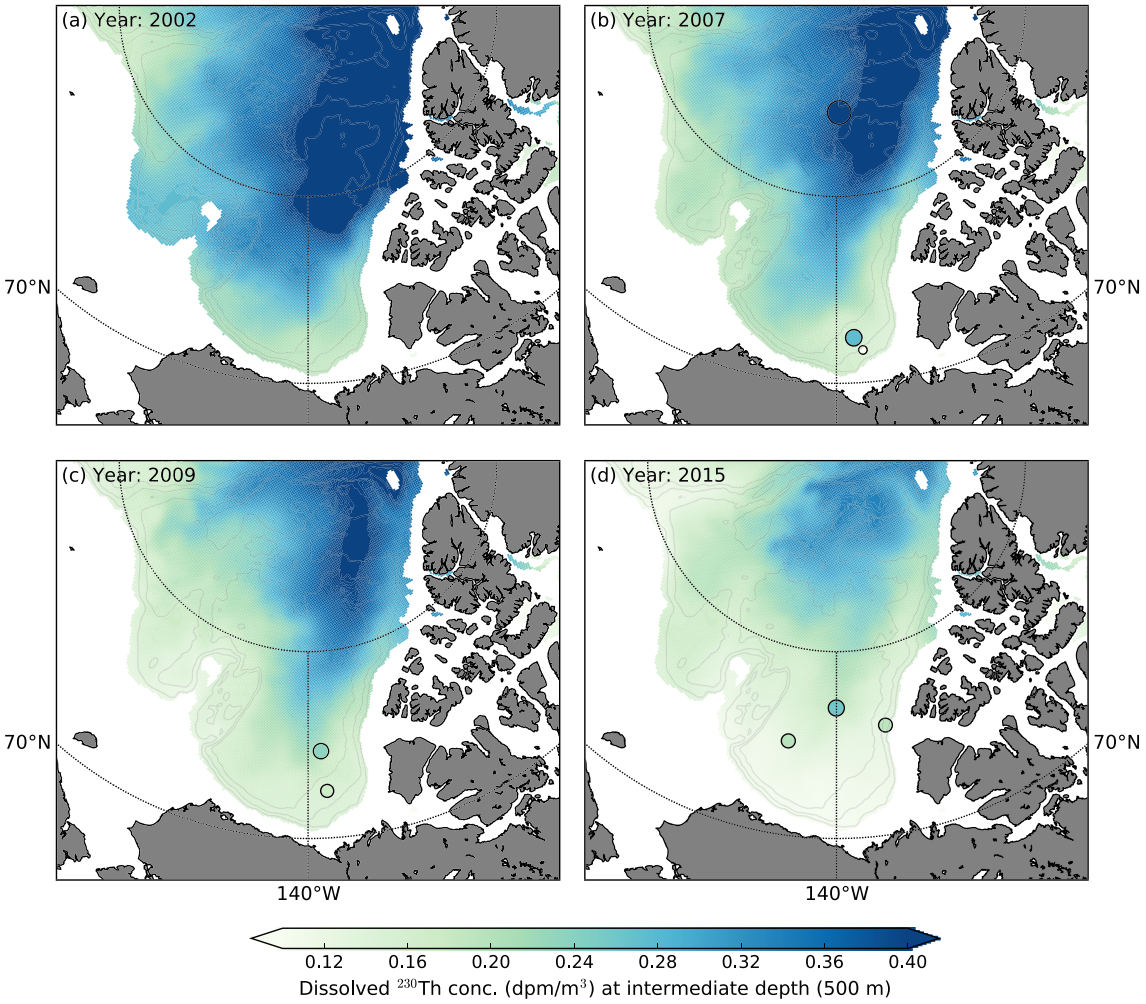


**Figure 4.** Yearly averages of modeled $^{230}$Th at 500 m depth in the core of the Atlantic layer across the Canada Basin in (a) 2002, (b) 2007, (c) 2009, and (d) 2015. Circles are observations; color and size of the circle reflect the value of $^{230}$Th concentration from vertical linear interpolation of closest values in the profile above and below that depth.

they will be referred as "shallow water" and "deep basin" in the rest of the paper. This division also allows us to use our well resolved model to investigate the role of boundary scavenging on the interior ocean.

To assess the origin of the $^{230}$Th decrease, we turn to the sensitivity experiments, one with constant ocean flows to assess the impact of changing ice on scavenging (Exp. 2) and one with constant ice to assess the impact of changing ocean flows, especially those in the warm Atlantic layer (Exp. 3). Here we note that the sea ice model coupled to the ocean model is not used to drive the tracer model, rather we use observations. Thus, in the model framework it is possible to split the impact of decreasing ice on the scavenging and the impact of decreasing ice on the ocean flows as the modeled sea ice affects modeled circulation while observed sea ice affects the particle flux.

The decrease in yearly average $^{230}$Th at 500 m depth between 2002 and 2014, averaged over the shallow and deep regions of the Canada Basin approaches 50% (Base Run, Figure 5). The tracer concentration in the deep basin drops more than the tracer concentration in the shallow regions. If the ice and thus the particle concentrations change but not the ocean flows (Exp. 2), over half of the decrease in the shallow regions is reproduced but only a 30% decrease is seen in the deep regions. The impact of the changes in ocean flows can be seen as the difference between the Base Run and Exp. 3 (Figure 5b).

In Exp. 2, the scavenging increases in time due to decreases in ice concentration, which is associated with increases in the particle field and represents increases in biological productivity. In this experiment, the $^{230}$Th concentration at 500 m depth decreases greatly with time, indicating a significant loss in $^{230}$Th as a

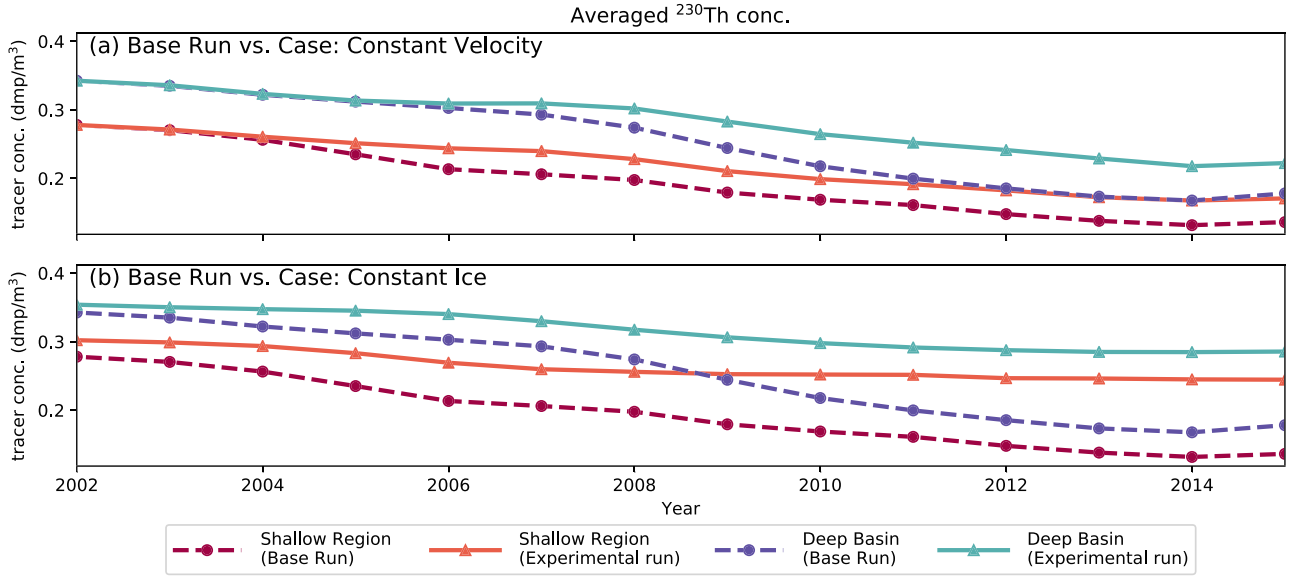


**Figure 5.** Time series of $^{230}$Th concentrations in different areas in the Canada Basin. (a) Base Run versus Exp. 2, in which the ocean flow repeats 2002 and thus does not change with time. Differences between two runs can be considered as the influence from the ocean flow. (b) Base Run versus Exp.3, where the sea ice is held at the 2002 level.

response to the loss of summer sea ice (Figure 5a). The impact from scavenging is stronger in the shallow region than the deep basin and thus, the gradient between the two regions is largely maintained in Exp. 2. On the contrary, in Base Run, the $^{230}$Th gradient is strongly reduced by the end of the time series. The difference between the runs, that is the impact of changes in ocean flow given the change in scavenging, only starts in 2004. From 2007–2013, the difference grows significantly with time in the deep basin only, implying that ocean flow has a much larger impact on $^{230}$Th in the ocean basin than in the shallow region.

In Exp. 3, where the ice concentration, and thus the particle concentration, was held constant, the tracer concentration drops about 20% by the end of the run (Figure 5b). In this experiment, the degree of decrease is equally significant in both regions. It suggests that without an increase in scavenging, the changes in ocean flow have a similar impact on both regions. As the percentage drop is similar, the gradient between the deep and shallow regions is also reduced.

Thus, in the Atlantic layer, the primary impact on the shallow region tracers is due to the increase in scavenging, whereas in the deep region is it partially due to the increase in scavenging, but also significantly decreased by changes in ocean circulation. The percentage decrease in both regions is similar, and thus the gradient between the two regions is decreased.

## 4. Discussion

### 4.1. Model Performance

Vertical profiles of observed and modeled results presented in Figure 3 provide an assessment of the simulation of $^{230}$Th. With or without the bottom scavenging component, the modeled $^{230}$Th concentration demonstrates consistency with observations in the Atlantic layer. In a quantitative way, the statistical analysis with a linear regression slope close to one illustrates that the model is in good agreement with the observations. Thus the model has high enough performance that it is useful and allows further tracer analysis.

However, if we focus on a deeper layer, the story is slightly different. In order to simulate an important feature revealed by the observed vertical deep profiles, that the rate at which the $^{230}$Th concentration increases with depth in the profile usually decreases in the last thousand meters, an additional scavenging component was added that improved the evaluation against observations. Previous modeling efforts in the Atlantic Ocean use general scavenging and physical mixing/advection in $^{230}$Th modeling but the bottom scavenging is not normally included (Lippold et al., 2012; Luo et al., 2010; Marchal et al., 2000). However, as the ocean dynamics are comparably weaker in the Arctic Ocean relative to lower latitudes, the effect from the

bottom scavenging is more prominent in the Arctic Ocean. Model and data comparison from vertical profiles in Figure 3 indicates that with this extra component added (solid lines), the linear regression line is brought much closer to the reference one-to-one line, suggesting that the nepheloid scavenging is a necessary component in Arctic $^{230}$Th modeling.

### 4.2. Reasons for a Decrease in $^{230}$Th

Both observations and modeling results suggest a reduction in $^{230}$Th across the Atlantic layer in recent years. Our analysis proposes that there are two factors responsible for this large scale $^{230}$Th reduction. First, this reduction is a result of the significant decrease in the summer sea ice concentration, regardless the choice of mixing, as supported by declines in $^{230}$Th concentrations from both the Base Run and Exp 2. (Figure 5). The recent ice reduction directly increases the amount of light that is allowed to penetrate through the water column, boosts primary production, and thus through our parametrization leads to an increase in particle flux, increasing $^{230}$Th scavenging. However, in addition to the impact of sea ice loss, winds can stimulate surface mixing and the associated nutrient upwelling enhances primary production and particle export in the Beaufort Sea (Castro de la Guardia et al., 2019); this process is not included in our parametrization. With the rise in the particle concentration level, the $^{230}$Th in the water column decreases due to the increase in scavenging. The second reason that helps to explain the $^{230}$Th reduction comes from enhanced circulation and mesoscale eddy mixing.

As well as the general decrease in $^{230}$Th concentrations, we also see a decrease in the gradient of $^{230}$Th in Atlantic layer between the continental margin and the deep ocean (Figure 4). The mixing/stirring process in the physical model in the Atlantic layer increases over the time of the simulation. The tracer model is forced with 5-day mean fields. The horizontal velocities in these fields stir the water masses and thus the $^{230}$Th. If the gradients in tracers such as $^{230}$Th are decreasing, we would expect to see the kinetic energy (KE) in the fluctuating field increasing. Note that as we are working with 5-day averages and grid sizes of 7 km, this would be the mesoscale eddy field. Thus we calculated:

$$KE = \frac{1}{A}\int (u-\bar{u})^2 + (v-\bar{v})^2 \mathrm{d}A \tag{11}$$

where $A$ is area, $(u, v)$ are the 5-day average velocities and $(\bar{u}, \bar{v})$ are the mean velocities over the year. The integral is done separately over the shallow and deep areas of the Canada Basin (see Figure 1).

The ocean mixing, quantified by the magnitude of kinetic energy per unit volume (KE), experiences an increase in both the shallow region and the deep basin (Figure 6). For the shallow Canada Basin, the mixing strength gently increases with time. A doubling in the mixing intensity occurs with a slight relaxation in 2014. Concurrently, the mixing in the deep basin undergoes an even more significant increase. By 2014, it is four times larger in magnitude than it was a decade previously. Moreover, the mixing in the shallow water and the deep basin is similar in strength by the end of the timeseries.

Note that the increase in the mixing strength from the physical fields occurs simultaneously with the decrease in $^{230}$Th in the deep basin in Exp. 3 (Figure 5b). The increase in the ocean basin mixing increases exchange between adjacent water masses. Figure 5 illustrates that the more dynamic physical field, including both advection and mixing, accounts for 30% of the total amount that $^{230}$Th decreases in the open ocean. The $^{230}$Th is more uniform between the deep and shallow ocean by the end of the simulation (Figure 4).

### 4.3. Drivers of Changes in $^{230}$Th in the Atlantic Layer of the Canada Basin

To look at the net changes in the Atlantic layer over the time of the simulation, we use the sum of equations (1) and (2), integrated over a region and a year. We calculate the terms that drive the changes in tracer in the coastal ocean and the deep basin (Figure 1)

$$Vx_{tot}\big|_{py}^{ny} = qV + A\left(sx_p\right)\big|_{bot}^{top} + \int_{boundary} x_{tot}\vec{u}\cdot\hat{n}\mathrm{d}A + \text{short time scale processes} \tag{12}$$

where $x_{tot} = x_p + x_d$, $V$ is the volume of the layer, $A$ is the horizontal area, $py$ and $ny$ are the previous year and next year, respectively, $top$ and $bot$ are the top and bottom of the layer, respectively, $t$ is one year and the flux integral is over the whole boundary of the layer with $\hat{n}$ being the outward normal to the boundary. All terms in equation (12) can be easily evaluated from the model results except the last one. We will infer it by the difference between the sum of the other terms on the right hand side and the net change seen (the left hand side). Processes at time scales less than 1 year include water mass stirring by mesoscale eddies,

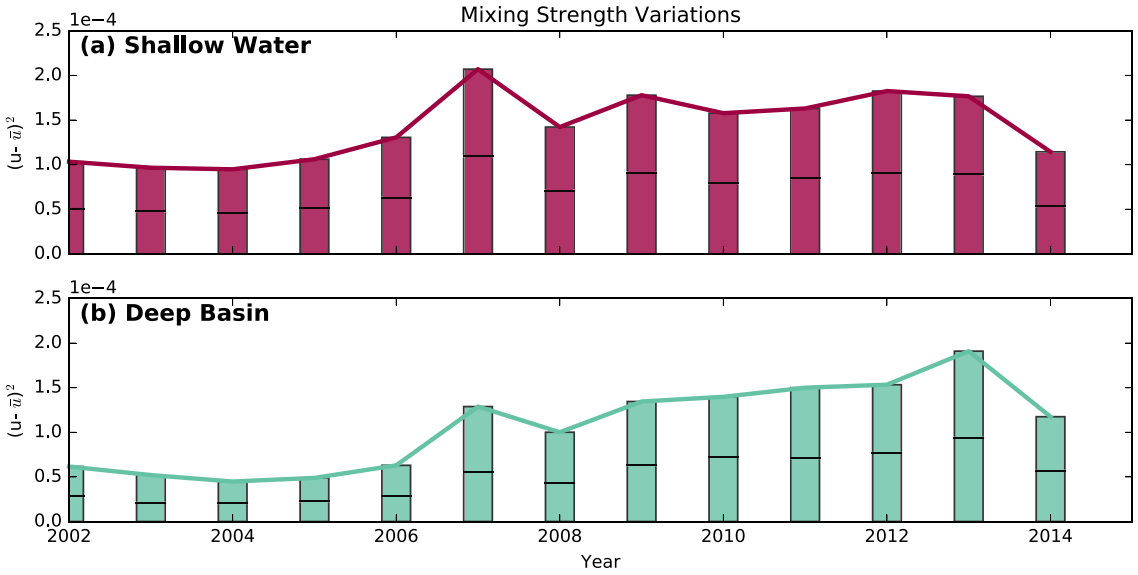


**Figure 6.** Time series of mixing strength (mean square 5-day velocities compared to the yearly means) in (a) the shallow region (defined as area shallower than 3,000 m; see Figure 1) and (b) the deep basin. The mixing in both zones increases with time, but the increase in the deep basin is more significant.

irreversible mixing facilitated by turbulence and any nonlinear seasonal variations in the sinking. These short time scale processes are included in the model but not in explicit terms in the time-integrated analysis of equation (12). A time series by year was calculated but the results integrated over the whole simulation are less noisy. We will focus on the integrated results as they reveal the processes more clearly.

As changes in $^{230}$Th are partially associated with changes in circulation and mixing, we evaluated the various advection terms, as well as the source of $^{230}$Th production (by $^{234}$U radioactive decay) and the $^{230}$Th sink from particle scavenging, and compared to the observed changes between 2002 and 2014, using equation (12). We separate the total advection into two components: that into the regions from the outside the Canada Basin and that between the regions inside the Canada Basin (Figure 7). As expected we see a stronger $^{230}$Th sink from particle scavenging than source from $^{230}$Th radioactive production in both shallow and deep areas. This difference is the signature of the enhanced scavenging due to the reduction in sea ice.

Again, we focus on the core of the Atlantic layer at approximately 500 m (specifically the model layer between 496 and 590 m). In this layer, the shallow region receives $^{230}$Th from the deep region and exports it out of the Canada Basin (Figure 7). This last term is due to the higher $^{230}$Th concentrations in the boundary current along the Canadian Arctic Archipelago than in the incoming boundary current along the Mendeleev Ridge (Figure 7). These two terms almost cancel and so the net advective component is small. The net loss in $^{230}$Th in the shallow region is explained largely by changes in scavenging. The observed change is well approximated by the yearly averaged terms, suggesting that the shorter time scale processes, such as mesoscale stirring, are small or nearly cancel. We suggest they nearly cancel, with the stirring mirroring the advection. The shallow region should gain $^{230}$Th from the deep region but lose it to the exterior, primarily through stirring along the Mendeleev Ridge. Although the $^{230}$Th gradients at the boundary along the Mendeleev Ridge are small horizontally (Figure 7), the isopycnals in this region slope down toward the Canada Basin, and thus the isopycnal $^{230}$Th gradient is large and inward (not shown) and therefore in the correct direction for isopycnal stirring to reduce $^{230}$Th in the Canada Basin.

In the same layer, the deep region exports $^{230}$Th to the shallow region. Advection from outside is small in the early years, but becomes weakly positive toward the end of the timeseries (not shown). Thus, in the deep region, losses are both due to scavenging and a net advection out of the region (Figure 7). The observed losses in $^{230}$Th are larger than we can explain with the estimated terms, pointing to significant shorter timescale processes. We suggest these processes are primarily mesoscale stirring between the deep region and the shallow region. Mesoscale eddies are a common feature of the water column between 500–2,000 m in the Canada Basin (Carpenter & Timmermans, 2012) and we suggest stirring by the model representations of these eddies is the missing loss term. The general features of the circulation in the core of the Atlantic

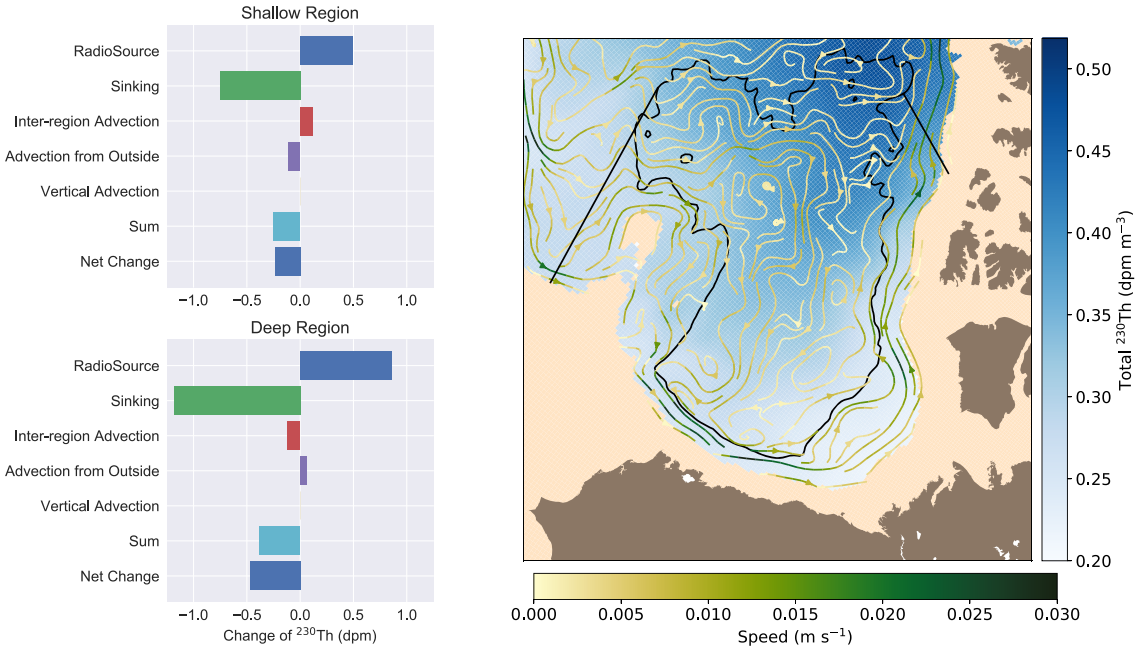


**Figure 7.** (left column) Modeled net fluxes from 2002–2015, for the shallow region (top) and the deep region (bottom) as defined in Figure 1, for the depth slice between 496 and 590 m. In both regions there is an imbalance between the production of $^{230}$Th by radioactive decay and the sinking through particle scavenging. In the shallow region, this directly leads to the net change in concentration as the advective fluxes are nearly balanced. In the deep region, advection also causes decreases in the concentration. (right panel) Mean circulation and $^{230}$Th concentration in the 500 m depth layer. Total $^{230}$Th concentration averaged from 2003–2015, contoured in blues (right color bar) and mean circulation as stream paths. Note that speed is given by color: yellow to green (lower color bar), not by distance between the stream paths. Black lines delineate the deep and shallow region, showing the defined edges (straight) and the 3,000 m isobath. Note the main fluxes into the shallow region from outside at the Mendeleev Ridge (left black line), and from the deep region at the southeast corner of the Northwind Ridge and main flux out along the Canadian Arctic Archipelago at the top right of the figure.

layer, and in particular, the anticyclonic circulation in the central part of the Canada Basin (Figure 7), are in agreement with geostrophic currents that were calculated deeper in the layer, at about 950 m depth, from salinity and temperature observations (Dosser & Timmermans, 2018).

Figure 7 shows the important impact of increased circulation and mesoscale stirring on the Atlantic layer. This result is in agreement with the strengthened mixing intensity over the Canada Basin (Figure 6), thus illustrating the usefulness of $^{230}$Th observations in revealing changes in ocean dynamics. Regarding reasons for increased mixing intensity, it is reasonable to believe that increased wind stress on the ocean is responsible. Increased wind stress can be due to a general increase in wind strength and/or reduced ice cover enabling more energy to penetrate into the ocean. Unlike the particle flux due to biological productivity, which is related to minimum summer ice, net wind stress into the ocean will depend on open water throughout the year. Increases in yearly mean ice free water in the Beaufort Sea are less significant than increases in the summer open water, but are still on order of 1.5% (Figure 8). An analysis of the winds over the Beaufort Sea shows that they themselves generally increased from 2003–2016 but that the net wind stress onto the ocean has increased more quickly (Figure 8). Interannual variations in wind stress onto the ocean are well correlated with the wind stress, not with the fraction of open water (Figure 8). Thus changes to wind stress into the ocean are caused not only by changes in ice cover in this region but also by changes of the strength of the winds (Figure 8). If winds continue to increase in the future, the mesoscale stirring will probably continue to increase and thus we can expect that the spatial variation of $^{230}$Th will continue to decrease in the Atlantic layer.

### 4.4. Model Limitations and Potential Future Improvements

Our model simulates the $^{230}$Th in the Canada Basin well but is less satisfactory in the Eurasian Basin and over the Mendeleev and Alpha Ridges where the sea ice coverage is consistently higher (Figure 3). $^{230}$Th modeling is very sensitive to the adsorption and desorption rates. We believe the discrepancies seen outside

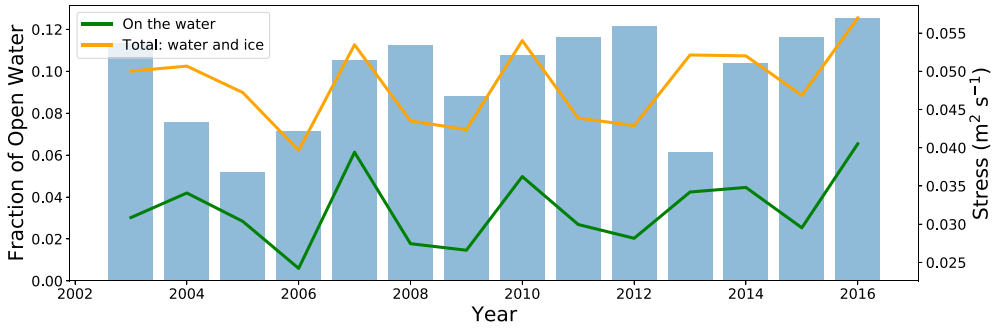


**Figure 8.** Wind stress changes over the Beaufort Sea. Mean yearly fraction of open water in the model (blue bars, scale on left). Wind stress over the Beaufort Sea is calculated from the winds forcing the model. Total wind stress ignoring ice/open water (orange line) and wind stress on the ocean accounting for changes in ice (green) with scale on right. Note that both increase over the time period but that the stress on the ocean increases slightly faster, consistent with the increasing open water. Specifically, the fraction of open water increased fastest over this period (2.5% per year, or 32% over the 13 years). The stress actually communicated to the ocean increased by 1% per year (13% over the 13 years), higher than the wind stress ignoring ice (0.6% or 8.2% over the 13 years). The interannual stress on the ocean is well correlated with the wind stress ignoring the ice, with correlation coefficient of 0.96, whereas it is very weakly correlated with the open water (correlation coefficient of 0.20).

of the Canada Basin are due to the simple linear relation between sea ice and scavenging. As an example, it is possible that the change in scavenging strength is very small for areas where the sea ice concentration is close to 0% or 100%, but is more significant for areas where the ocean is partially covered by ice (similar to an S Curve shape function). Other studies, in regions with more data, have used multiple types of particles, differentiating between, for example, opal from diatoms and lithogenic particles (Dutay et al., 2009; Van Hulten et al., 2018). More research and in particular, more observations, will be needed to better constrain the relation between sea ice and adsorption and desorption rates so that $^{230}$Th can be better simulated in the future.

In addition, compared to the Canada Basin, areas such as Eurasian Basin and Makarov Ridge are more sensitive to variations in the Atlantic inflow. The $^{230}$Th concentration carried by the Atlantic inflow probably varies with time but could not be incorporated due to the poor temporal and spatial coverage of $^{230}$Th observations. However, this uncertainty is not expected to be dominant. The most important model component to improve is the particle dynamics that drive the adsorption and desorption processes.

## 5. Conclusions

As a sensitive indicator to climate change, the Arctic Ocean is receiving increasing attention. Our study combines geotracer and modeling techniques to provide a new way to understand the changing Arctic Ocean circulation. There is an overall reduction in the $^{230}$Th concentration and spatial gradient in the Canada Basin. Sensitivity experiments suggest that, while a large amount of the reduction is due to increased particle fluxes from increased productivity due to reduced ice cover, the strengthening in the Atlantic layer circulation and mesoscale stirring also leads to a substantial decrease in the $^{230}$Th concentration, particularly in the deep regions (where the sea floor is deeper than 3,000 m). This increase in ocean velocities is probably due to more intensive wind energy input to the ocean.

To successfully simulate the $^{230}$Th, we had to include nepheloid scavenging. Our model also included a resolved continental shelf and slope region. We found that exchange between the deep basin and this region decreased $^{230}$Th in the deep basin. Thus, due to the high proportion of continental shelf and relatively weak dynamics compared to lower latitudes, our study suggests that nepheloid and boundary scavenging in the Arctic should not be overlooked. Otherwise, there is an overestimation of $^{230}$Th created by misinterpreting the scavenging intensity in the deep oceans as presented in Exp.1.

Ocean tracers such as $^{230}$Th integrate ocean processes and allow us to estimate large-scale, multidecadal changes in circulation and particle flux, illustrating the potential of geochemical tracers when combining spatiotemporal data sets with circulation models. Repeated measurements of $^{230}$Th over time in Canada Basin reveal changes in circulation and stirring, and in particle flux. Use of a numerical model provides

enhanced interpretation of the observations. With the gradual melting of sea ice expected in the coming decades, continued measurements of water column $^{230}$Th will provide unique insights into the evolution of productivity and circulation in the Arctic Ocean. Additional $^{230}$Th profiles measured along section GN01 of the GEOTRACES program in 2015 will also fill an important data gap and provide additional details on mixing and particle flux in the Northwind Ridge area and Makarov Basin. A similar approach is applicable to other oceanic regions where particle scavenging and seawater $^{230}$Th concentrations are spatially variable.

## Appendix A: Methods in Scavenging Coefficients Parametrization

In this study, scavenging coefficients were estimated using pre-2000s $^{230}$Th data as shown in Figure A1. For particulate $^{230}$Th, assuming a steady state is reached, equation (3) implies that the slope of the profile ($\alpha_p$) is directly related to the particle sinking speed:

$$s = \frac{q}{\alpha_p} \tag{A1}$$

Similarly, equation (4) indicates that a steady state dissolved $^{230}$Th profile has an intercept that is inversely related to the adsorption rate and a slope that is controlled by both the sinking speed and the ratio of desorption rate and adsorption rate. Provided the slope is $\alpha_d$, the ratio of adsorption rate over desorption rate can be found:

$$\frac{k_a}{k_d} = \frac{q}{\alpha_d s} = \frac{\alpha_p}{\alpha_d} \tag{A2}$$

Note that (A2) only provides a relationship between adsorption and desorption rates. As an earlier study (Bacon & Anderson, 1982) suggested that there is no strong correlation between the desorption rate coefficient and suspended matter concentration, we consider the $^{230}$Th desorption rate ($k_d$) as a constant over the Arctic. The rate is approximated by a $k_d$ value that produces the lowest discrepancy between observations and analytical solutions. With $k_d$ determined, the adsorption rate is available:

$$k_a = k_d \frac{\alpha_p}{\alpha_d} \tag{A3}$$

Particles in each Arctic basin should have similar sources, and thus stations that are geographically close are grouped together for the analysis (Figure A1). In the Eurasian Basin area, the sinking speed $s$ is estimated to be 960 m yr$^{-1}$, approximately 1.5 times higher than that found in the Alpha Ridge area, 615 m yr$^{-1}$. The

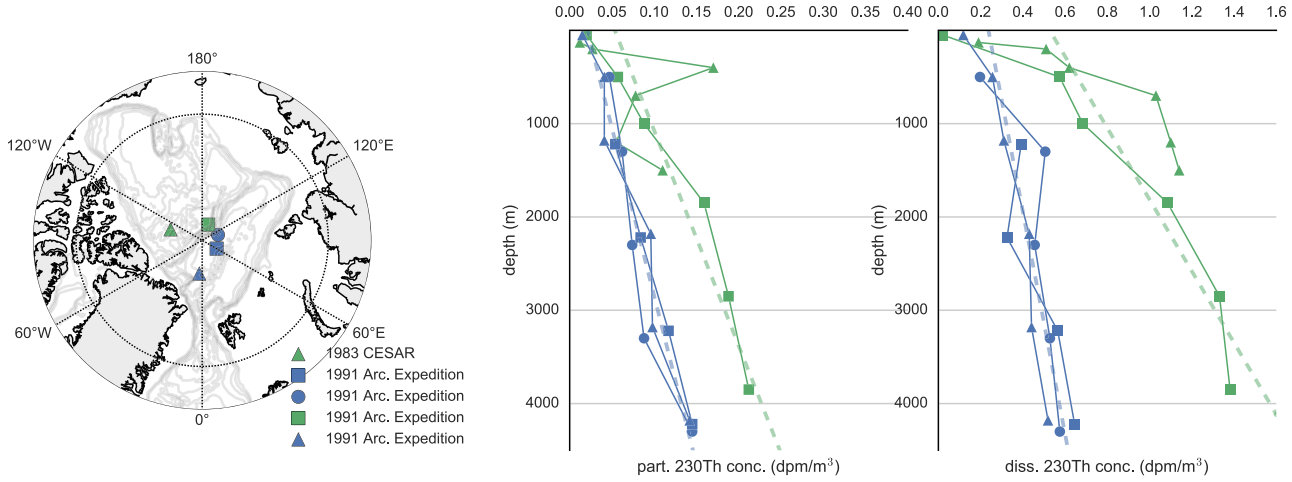


**Figure A1.** Linear regressions of the observed $^{230}$Th profiles in the Eurasian Basin and the Alpha Ridge region. (left panel) Map with observation locations. (middle panel) Linear regressions on observed particulate $^{230}$Th (Eurasian Basin—slope: $2.78 \times 10^{-5}$ dpm m$^{-4}$, intercept: 0.02 dpm m$^{-3}$; Alpha Ridge—slope: $4.33 \times 10^{-5}$ dpm m$^{-4}$, intercept: 0.05 dpm m$^{-3}$); (right panel) the same but for the dissolved $^{230}$Th profile (Eurasian Basin—slope: $8.38 \times 10^{-5}$ dpm m$^{-4}$, intercept:0.23 dpm m$^{-3}$; Alpha Ridge—slope: $2.61 \times 10^{-4}$ dpm m$^{-4}$, intercept: 0.52 dpm m$^{-4}$). Tracer profiles show that $^{230}$Th concentrations over the Alpha Ridge and in the Makarov Basin (green) increase with depth faster than those in the Eurasian Basin (blue).

estimated adsorption rate is about 0.13 $yr^{-1}$ for the Alpha Ridge area which is close to a previously reported value, 0.16 $yr^{-1}$ (Bacon et al., 1989). The adsorption rate in the Eurasian Basin is assessed to be 0.26 $yr^{-1}$, which is also within the range of 0.12 to 0.55 $yr^{-1}$ suggested by Trimble et al. (2004). The desorption rate, $k_d$, is chosen to be 0.8 $yr^{-1}$. Note that higher values are seen in the Eurasian Basin area for both sinking speed and absorption rate, compared to the Alpha Ridge. This difference implies particle dynamics are more active in the Eurasian Basin area, as expected, because primary production in the Arctic is strongly affected by sea ice through its control on light availability (Brown & Arrigo, 2012), and the Alpha Ridge area is covered by heavy sea ice.

Considering that the distribution of $^{230}$Th is closely related to particle concentration distribution (Bacon & Anderson, 1982), and that sea ice is one of the key drivers of primary production (especially by the summer minimum ice, because the major portion of biologic productivity occurs during the summer (Kim et al., 2015)), we conjecture that high biological productivity around the ice free margins of the Arctic Ocean creates a region of enhanced removal of trace elements by scavenging onto particles, while the low biological productivity area that sits under permanent ice produces a region of weak scavenging.

This conjecture implies a negative correlation between the scavenging coefficients and sea ice concentration, which enables a reasonable estimation of an Arctic-wide scavenging intensity by using the horizontal variations of the summer minimum sea ice concentration. Using historical sea ice data provided by NOAA/NSIDC Climate Data Record data set (Meier et al., 2013; Peng et al., 2013), relationships (5) and (6) are derived.

**Acknowledgments**
This work was funded through the Canadian GEOTRACES program, a project funded by Canadian Climate and Atmospheric Research. We would like to thank the Canadian GEOTRACES team for assistance in collecting the data and excellent discussions of the Arctic Ocean system. Technical help was provided by Doug Latornell and Maureen Soon. We thank Juliana Marson for the analysis of the winds and wind stress in the model. The off-line chemistry model results of this research are available at https://dataverse.scholarsportal.info/dataset.xhtml?persistentId=doi:10.5683/SP2/ZM89PF. The scripts that produced the analysis and figures and the Fortran modules for the tracer code are available from a bitbucket repository (at https://bitbucket.org/ccar-modeling/yuetal). We are grateful to the NEMO development team and the Drakkar project for providing the model and continuous guidance and to Westgrid and Compute Canada for computational resources, where all model experiments were performed and are archived (http://www.computecanada.ca). NEMO can be downloaded online (from https://www.nemo-ocean.eu/). Two anonymous reviewers provided detailed comments, and we thank them for helping us improve the manuscript.

## References

Anderson, R. F., Bacon, M. P., & Brewer, P. G. (1983). Removal of $^{230}$Th and $^{231}$Pa at ocean margins. *Earth and Planetary Science Letters*, *66*, 73–90.

Anderson, R. F., Fleisher, M. Q., Robinson, L., Edwards, R. L., Hoff, J. A., Moran, S. B., et al. (2012). GEOTRACES intercalibration of $^{230}$Th, $^{232}$Th, $^{231}$Pa, and prospects for $^{10}$Be. *Limnology and Oceanography-Methods*, *10*, 179–213.

Arrigo, K. R., van Dijken, G., & Pabi, S. (2008). Impact of a shrinking Arctic ice cover on marine primary production. *Geophysical Research Letters*, *35*, L19603. https://doi.org/10.1029/2008GL035028

Bacon, M. P. (1988). Tracers of chemical scavenging in the ocean: Boundary effects and large-scale chemical fractionation. *Philosophical Transactions of the Royal Society of London, Series A*, *325*, 147–160.

Bacon, M. P., & Anderson, R. F. (1982). Distribution of thorium isotopes between dissolved and particulate forms in the deep sea. *Journal of Geophysical Research*, *87*, 2045–2056.

Bacon, M. P., Huh, C.-A., & Moore, R. M. (1989). Vertical profiles of some natural radionuclides over the Alpha Ridge, Arctic ocean. *Earth and Planetary Science Letters*, *95*, 15–22.

Brown, Z. W., & Arrigo, K. R. (2012). Contrasting trends in sea ice and primary production in the Bering Sea and Arctic Ocean. *ICES Journal of Marine Science*, *69*(7), 1180–1193.

Carpenter, J., & Timmermans, M.-L. (2012). Deep mesoscale eddies in the Canada basin, Arctic Ocean. *Geophysical Research Letters*, *39*, L20602. https://doi.org/10.1029/2012GL053025

Castro de la Guardia, L., Garcia-Quintana, Y., Claret, M., Hu, X., Galbraith, E. D., & Myers, P. G. (2019). Assessing the role of high-frequency winds and sea ice loss on Arctic phytoplankton blooms in an ice-ocean-biogeochemical model. *Journal of Geophysical Research: Biogeosciences*, *124*, 2728–2750. https://doi.org/10.1029/2018JG004869

Core Writing Team (2014). *Climate change 2014: Synthesis report. Contribution of Working Groups I, II and III to the Fifth Assessment Report of the Intergovernmental Panel on Climate Change Edited by* R. K. Pachauri, & L. A. Meyer, pp. 151. Geneva, Switzerland: IPCC.

Courtois, P., Hu, X., Pennelly, C., Spence, P., & Myers, P. G. (2017). Mixed layer depth calculation in deep convection regions in ocean numerical models. *Ocean Modelling*, *120*, 60–78.

Dai, A., Qian, T., Trenberth, K. E., & Milliman, J. D. (2009). Changes in continental freshwater discharge from 1948 to 2004. *Journal of Climate*, *22*, 2773–2792.

Dosser, H. V., & Timmermans, M. (2018). Inferring circulation and lateral eddy fluxes in the Arctic Ocean's deep Canada basin using an inverse method. *Journal of Physical Oceanography*, *48*, 245–260.

Dutay, J.-C., Lacan, F., Roy-Barman, M., & Bopp, L. (2009). Influence of particle size and type on $^{231}$Pa and $^{230}$Th simulation with a global coupled biogeochemical-ocean general circulation model: A first approach. *Geochemistry, Geophysics, Geosystems*, *10*, Q01011. https://doi.org/10.1029/2008GC002291

Edmonds, H. N., Moran, S. B., Hoff, J. A., Smith, J. N., & Edwards, R. L. (1998). Protactinium-231 and Thorium-230 abundances and high scavenging rates in the western Arctic Ocean. *Science*, *205*, 405–407.

Grenier, M., Francois, R., Soon, M., Rutgers van der Loeff, M., Yu, X., Valk, O., et al. (2019). *Changes of circulations and particle scavenging in the Amerasian Basin of the Arctic Ocean inferred from the distribution of radioactive and radiogenic tracers in the last three decades*, vol. 124, pp. 9338–9363. https://doi.org/10.1029/2019JC015265

Henderson, G., & Wilkinson, J. (2012). Global database of literature and unpublished water column Pa and Th data. Retrieved from http://climotope.earth.ox.ac.uk/data_compilations/water-column_th_and_pa_dataset_notes_and_references.

Hill, V. J., Matrai, P. A., Olson, E., Suttles, S., Steele, M., Codispoti, L., & Zimmerman, R. C. (2013). Synthesis of integrated primary production in the Arctic Ocean: II. In situ and remotely sensed estimates. *Progress in Oceanography*, *110*, 107–125.

Hu, X., Sun, J., Chan, T. O., & Myers, P. G. (2018). Thermodynamic and dynamic ice thickness contributions in the Canadian Arctic Archipelago in NEMO-LIM2 numerical simulations. *Cryosphere*, *12*(4), 1233–1247. https://doi.org/10.5194/tc-12-1233-2018

Hunkins, K., Thorndike, E. M., & Mathieu, G. (1969). Nepheloid layers and bottom currents in the Arctic Ocean. *Journal of Geophysical Research*, *74*(28), 6995–7008. https://doi.org/10.1029/jc074i028p06995

Ilicak, M., Drange, H., Wang, Q., Gerdes, R., Aksenov, Y., Bailey, D., et al. (2016). An assessment of the Arctic Ocean in a suite of interannual CORE-II simulations. Part III: Hydrography and fluxes. *Ocean Modelling*, *100*, 141–161. https://doi.org/10.1016/j.ocemod.2016.02.004

Jackson, J., Allen, S., Carmack, E., & McLaughlin, F. (2010). Suspended particles in the Canada basin from optical and bottle data, 2003–2008. *Ocean Science*, *6*(3), 799–813.

Karcher, M., Smith, J. N., Kauker, F., Gerdes, R., & Smethie Jr, W. M. (2012). Recent changes in Arctic Ocean circulation revealed by iodine-129 observations and modeling. *Journal of Geophysical Research*, *117*, C08007. https://doi.org/10.1029/2011JC007513.

Kim, M., Hwang, J., Kim, H. J., Kim, D., Yang, E. J., Ducklow, H. W., et al. (2015). Sinking particle flux in the sea ice zone of the Amundsen shelf, Antarctica. *Deep-Sea Research Part I*, *101*, 110–117.

Lerner, P., Marchal, O., Lam, P. J., Anderson, R. F., Buesseler, K., Charette, M. A., et al. (2016). Testing models of thorium and particle cycling in the ocean using data from station GT11-22 of the US GEOTRACES north Atlantic section. *Deep-Sea Research Part I*, *113*, 57–79.

Lippold, J., Luo, Y., Francois, R., Allen, S. E., Gherardi, J., Pichat, S., et al. (2012). Strength and geometry of the glacial Atlantic meridional overturning circulation. *Nature Geoscience*, *5*(11), 813–816.

Lique, C., Treguier, A.-M., Blanke, B., & Grima, N. (2010). On the origins of water masses exported along both sides of Greenland: A Lagrangian model analysis. *Journal of Geophysical Research*, *115*, C05019. https://doi.org/10.1029/2009JC005316

Luo, Y., Francois, R., & Allen, S. E. (2010). Sediment $^{231}$Pa/$^{230}$Th as a recorder of the rate of the Atlantic meridional overturning circulation: Insights from a 2-D model. *Ocean Science*, *6*, 381–400.

Luo, Y., & Lippold, J. (2015). Controls on $^{231}$Pa and $^{230}$Th in the Arctic ocean. *Geophysical Research Letters*, *42*, 5942–5949. https://doi.org/10.1002/2015GL064671

Madec, G., & The NEMO team (2016). NEMO Ocean Engine (*1288-1619*). France: Institut Pierre-Simon Laplace (IPSL). Available at http://www.nemo-ocean.eu/content/download/180742/735839/file/NEMO&urluscore;book&urluscore;3.6&urluscore;STABLE.pdf

Marchal, O., Franċois, R., Stocker, T. F., & Joos, F. (2000). Ocean thermohaline circulation and sedimentary $^{231}$Pa/$^{230}$Th ratio. *Paleoceanography*, *15*(6), 625–641.

Marchal, O., François, R., & Scholten, J. (2007). Contribution of $^{230}$Th measurements to the estimation of the abyssal circulation. *Deep-Sea Research Part I*, *54*(4), 557–585.

McLaughlin, F. A., Carmack, E. C., Williams, W. J., Zimmermann, S., Shimada, K., & Itoh, M. (2009). Joint effects of boundary currents and thermohaline intrusions on the warming of Atlantic water in the Canada Basin, 1993–2007. *Journal of Geophysical Research*, *114*, C00A12. https://doi.org/10.1029/2008JC005001

Meier, W., Fetterer, F., Savoie, M., Mallory, S., Duerr, R., & Stroeve, J. (2013). Climate data record of passive microwave sea ice concentration, version 2. Boulder, Colorado, USA: NOAA/NSIDC.

Muilwijk, M., Smedsrud, L. H., & Meyer, A. (2016). Bottom melting of Arctic Sea Ice in the Nansen Basin due to Atlantic Water influence. In *EGU Gen. Assembly Abstr*, *18*, pp. EPSC2016–268.

Peng, G., Meier, W., Scott, D., & Savoie, M. (2013). A long-term and reproducible passive microwave sea ice concentration data record for climate studies and monitoring. *Earth System Science Data*, *5*(2), 311–318.

Rempfer, J., Stocker, T. F., Joos, F., Lippold, J., & Jaccard, S. L. (2017). New insights into cycling of $^{231}$Pa and $^{230}$Th in the Atlantic Ocean. *Earth and Planetary Science Letters*, *468*, 27–37. https://doi.org/10.1016/j.epsl.2017.03.027

Roy-Barman, M. (2009). Modelling the effect of boundary scavenging on thorium and protactinium profiles in the ocean. *Biogeosciences*, *6*(12), 3091–3107.

Rudels, B., Jones, E. P., Schauer, U., & Eriksson, P. (2004). Atlantic sources of the Arctic Ocean surface and halocline waters. *Polar Research*, *23*, 181–208.

Scholten, J., Van Der Loe, M. R., & Michel, A. (1995). Distribution of $^{230}$Th and $^{231}$Pa in the water column in relation to the ventilation of the deep Arctic basins. *Deep Sea Research Part II*, *42*, 1519–1531. https://doi.org/0967-0645(95)000524

Serreze, M. C., Stroeve, J., Barrett, A. P., & Boisvert, L. N. (2016). Summer atmospheric circulation anomalies over the Arctic Ocean and their influences on September sea ice extent: A cautionary tale. *Journal of Geophysical Research: Atmospheres*, *121*, 11,463–11,485. https://doi.org/10.1002/2016JD025161

Smith, G. C., Roy, F., Mann, P., Dupont, F., Brasnett, B., Lemieux, J.-F., et al. (2014). A new atmospheric dataset for forcing ice–ocean models: Evaluation of reforecasts using the Canadian global deterministic prediction system. *Quarterly Journal of the Royal Meteorological Society*, *140*(680), 881–894.

Tanhua, T., Jones, E. P., Jeansson, E., Jutterström, S., Smethie, W. M., Wallace, D. W., & Anderson, L. G. (2009). Ventilation of the Arctic Ocean: Mean ages and inventories of anthropogenic $CO_2$ and CFC-11. *Journal of Geophysical Research*, *114*, C01002. https://doi.org/10.1029/2008JC004868

Trimble, S., Baskaran, M., & Porcelli, D. (2004). Scavenging of thorium isotopes in the Canada Basin of the Arctic Ocean. *Earth and Planetary Science Letters*, *222*(3), 915–932.

Valk, O., van der Loeff, M. M. R., Geibert, W., Gdaniec, S., Rijkenberg, M. J. A., Moran, S. B., et al. (2018). Importance of hydrothermal vents in scavenging removal of $^{230}$Th in the Nansen Basin. *Geophysical Research Letters*, *45*, 10,539–10,548. https://doi.org/10.1029/2018GL079829

Van Hulten, M., Dutay, J.-C., & Roy-Barman, M. (2018). A global scavenging and circulation ocean model of thorium-230 and protactinium-231 with improved particle dynamics (NEMO–prothorp 0.1). *Geoscientific Model Development*, *11*(9), 3537–3556.

Wang, Q., Ilicak, M., Gerdes, R., Drange, H., Aksenov, Y., Bailey, D. A., et al. (2016b). An assessment of the Arctic Ocean in a suite of interannual CORE-II simulations. Part I: Sea ice and solid freshwater. *Ocean Modelling*, *99*, 110–132. https://doi.org/10.1016/j.ocemod.2015.12.008

Wang, Q., Ilicak, M., Gerdes, R., Drange, H., Aksenov, Y., Bailey, D. A., et al. (2016a). An assessment of the Arctic Ocean in a suite of interannual CORE-II simulations. Part II: Liquid freshwater. *Ocean Modelling*, *99*, 86–109. https://doi.org/10.1016/j.ocemod.2015.12.009

Woodgate, R. A., Aagaard, K., Swift, J. H., Smethie Jr., W. M., & Falkner, K. K. (2007). Atlantic water circulation over the Mendeleev Ridge and Chukchi Borderland from thermohaline intrusions and water mass properties. *Journal of Geophysical Research*, *112*, C02005. https://doi.org/10.1029/2005JC003416

Yu, X. (2017). Modeling $^{230}$Th (and $^{231}$Pa): As an approach to study the intermediate and deep water circulation in the Arctic Ocean (Master's thesis), University of British Columbia.

Yu, E.-F., Francois, R., & Bacon, M. P. (1996). Similar rates of modern and last-glacial ocean thermohaline circulation inferred from radiochemical data. *Nature*, *379*(6567), 689.